

## THREE CANDIDATE CLUSTERS AROUND HIGH REDSHIFT RADIO-LOUD SOURCES: MG1 J04426+0202, 3C 068.2, AND MS 1426.9+1052

J. R. FRANCK<sup>1</sup>, S. S. MCGAUGH<sup>1</sup>, AND J. M. SCHOMBERT<sup>2</sup><sup>1</sup>Case Western Reserve University, 10900 Euclid Ave., Cleveland, OH 44106, USA<sup>2</sup>University of Oregon, 1585 E. 13th Ave., Eugene, OR 97403, USA

Received 2014 September 2; accepted 2015 May 28; published 2015 July 15

## ABSTRACT

We present near-infrared observations of the environments around three radio-loud sources (MG1 J0442+0202, 3C 068.2, and MS 1426.9+1052) at redshifts  $z = 1.10, 1.57,$  and  $1.83$  (respectively) that are surrounded by near-infrared galaxy overdensities. Overdensities with respect to field counts were found to be significant up to  $19\sigma$ , with 12 times the expected number of galaxies within the inner regions of the densest proto-cluster. Color-magnitude relations are constructed in  $K_s, J - K_s$ , with each candidate cluster exhibiting a feature consistent with the beginnings of a red sequence (RS). Galaxy models based on the redshift of the radio source are used to compare expected CMRs for a given formation epoch with the observed RS of each candidate, and are found to be consistent with an old ( $z_f > 5$ ) formation epoch for a few bright, red galaxies on the RS.

*Key words:* galaxies: clusters: general – galaxies: clusters: individual (CL J0442+0202, 3C 068.2, MS 1426.9+1052)

## 1. INTRODUCTION

The largest overdensities in the early universe are observed today as galaxy clusters. These initial density perturbations can be used as probes over a range of epochs for the cosmological parameters that characterize our universe (Cen & Ostriker 1994; Vikhlinin et al. 2009). Cluster observables (number density, mass) as a function of redshift provide constraints for  $\Omega_\Lambda$  and  $\Omega_m$ . The mass and formation timescale of high redshift clusters compared with simulations of large-scale structure is a powerful test of  $\Lambda$ CDM (Mortonson et al. 2011). Recent discoveries are challenging the boundaries at how rapidly large structures can form ( $z \sim 2$  from Gobat et al. 2013;  $z \sim 3.8$  from Lee et al. 2014a;  $z \sim 4$  from Venemans et al. 2002), and how massive they can become (e.g., “El Gordo”  $M > 10^{15} M_\odot$  at  $z \sim 0.9$  in Menanteau et al. 2012). Identification of the epoch of cluster formation is an important test of cosmology and the dark energy equation of state.

Previously these high redshift structures were identified via galaxy overdensities in near-infrared (NIR) photometric surveys (Stern et al. 2003; Eisenhardt et al. 2008; Papovich 2008; Papovich et al. 2010). Clusters are also associated around radio-loud sources (Hall et al. 2001) out to redshifts  $z \sim 4$  (Venemans et al. 2002). Utilizing the intracluster medium (ICM) as an identifier, diffuse X-ray emission has been useful in increasing the number of known high redshift clusters (Gobat et al. 2011; Willis et al. 2013), while the Sunyaev–Zel’Dovich (SZ) effect is becoming increasingly powerful with the success of the South Pole Telescope (Keisler et al. 2011), Atacama Cosmology Telescope (Sievers et al. 2013), the *Planck* satellite (Planck Collaboration et al. 2013a), and with the Combined Array for Research in Millimeter-wave Astronomy (CARMA;<sup>3</sup> Muchovej et al. 2007; Culverhouse et al. 2010; Mantz et al. 2014).

We present three cluster candidates at  $z > 1$ , two of which have not been identified previously. High-redshift radio-loud sources were targeted for NIR photometry to search for a galaxy overdensity in the surrounding region, which has

proven to be a robust identifier of structure (Stern et al. 2003; Haas et al. 2009; Galametz et al. 2010). Section 2 describes the NIR observations and photometry, while the overdensity associated with each cluster candidate is discussed in Section 3. The photometry of each candidate cluster is presented in Section 4 and analyzed in Section 5, with a summary presented in Section 6.

The work presented here assumes a  $\Lambda$ CDM concordance cosmology, with  $\Omega_\Lambda = 0.7$ , a matter density of  $\Omega_m = 0.3$ , and  $H_0 = 70 \text{ km s}^{-1} \text{ Mpc}^{-1}$ .

## 2. OBSERVATIONS

Three candidate clusters were observed with Kitt Peak National Observatory’s Mayall 4 m telescope equipped with the SQUIID Camera in the NIR  $J, H, K_s$  and  $L$  passbands between 2006 January to 2007 April. A summary of observations can be found in Table 1. Each passband is projected onto a  $440 \times 460$  pixel InSb detector (covering  $172'' \times 179''$  in R.A./Decl.). Individual frames were co-added and corrected for cosmic rays with the IRAF<sup>4</sup> (Tody 1986, 1993) *IMCOMBINE* routine.

The candidate cluster around 3C 068.2 was also imaged with the NEWFIRM camera on the 4 m in 2008 October. NEWFIRM is a wide-field camera that spans  $28' \times 28'$ , and images were taken in  $J, H,$  and  $K_s$  filters. The cluster fell entirely within one quadrant of the NEWFIRM camera, so we devised the “four-shooter” observational mode in which the telescope is shifted from quadrant to quadrant to maximize time on target while simultaneously observing sky. These frames were processed by the NEWFIRM Quick-reduce Pipeline. The galaxy photometry between the NEWFIRM and SQUIID images were within the photometric errors, increasing our confidence in the calibration and detection procedures.

<sup>4</sup> IRAF is distributed by the National Optical Astronomy Observatories, which are operated by the Association of Universities for Research in Astronomy, Inc., under cooperative agreement with the National Science Foundation.

<sup>3</sup> <http://www.mmarray.org>

**Table 1**  
Observation Log

Date	Field	Instrument	Bands	Typical Seeing
2006 January 7–9	CL J0442+0202	SQIID	$J, H, K_s, L$	0"5–0"8
2006 January 7–9	3C 068.2	SQIID	$J, H, K_s, L$	0"5–0"8
2007 April 7–9	MS 1426.9+1052	SQIID	$J, H, K_s, L$	1"1
2008 October 12–13	3C 068.2	NEWFIRM	$J, H, K_s$	1"1–1"3

**Note.** Observation summary for the three selected candidate clusters.

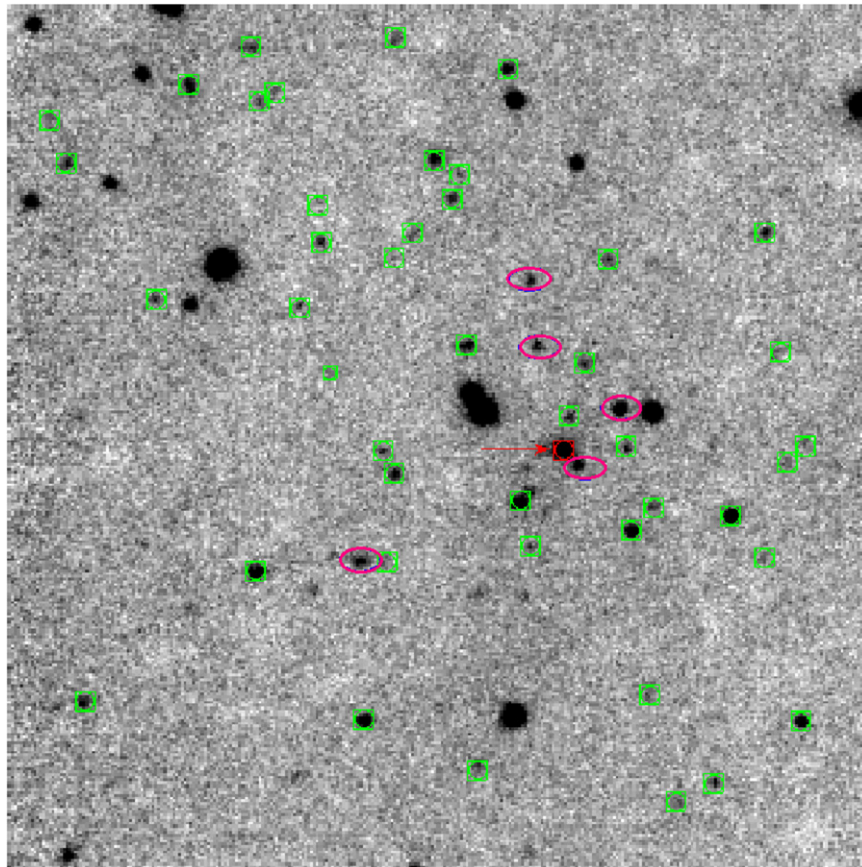


**Figure 1.** SQIID  $K_s$  image of CL J0442+0202, which spans  $120'' \times 120''$ . The radio source MG1 J04426+0202 is indicated by a red arrow and square, while spectroscopically confirmed cluster members (Stern et al. 2003) are inside magenta ellipses. The green boxes are the remainder of the sources measured photometrically.

Sky subtraction was accomplished by chopping on and off field while dithering between frames. The resulting sky flats displayed variations of only 0.02% based on sky box determination of the frame sky value. Hysteresis from a bright star in the  $K_s$  frames for cluster MS 1426.9+1052 produced some large-scale features (visible under high contrast; see Figure 5). However, these variations are less than 0.04% of the background and do not affect the galaxy photometry routines that used local sky. Both  $J$  and  $K_s$  frames were used for galaxy identification and each object was confirmed visually in both frames before inclusion in our analysis.

Calibration of the stacked images utilized the 2MASS Point Source Catalog for stars within the individual frames in the  $J$  and  $K_s$  filters. With the wide field of view (FOV) of NEWFIRM, a large sample of stellar sources was used for calibration (474 matches for  $J$  and 577 stars for  $K_s$ ), providing photometric solutions with intrinsic scatter of  $\sigma_J = 0.05$  mag and  $\sigma_{K_s} = 0.09$  mag. A photometric solution for the SQIID

instrument was found in a similar way, but the smaller FOV of each image provided fewer 2MASS calibration sources. CL J0442+0202 and 3C 068.2 were imaged on the same run in 2006 January, while MS 1426.9+1052 was observed in 2007 April. Unfortunately, no usable 2MASS stars were in the latter field, so the photometric solutions for MS 1426.9+1052 were derived using 2MASS stars within other science frames taken during the 2007 April run.

Source Extractor (SExtractor; Bertin & Arnouts 1996) was used to create an initial list of sources from both  $J$  and  $K_s$  frames. Galaxies and stars were distinguished using the stellar index parameter. A few of the faintest objects were below the detection threshold in one filter (typically  $J$ ) and were confirmed visually in both filters. A few objects were visible in the  $K_s$  frames, but rejected as they were below the threshold or not visible in the  $J$  frame, preventing a color determination. The final set of objects are marked in Figures 1, 3, and 5, all clearly visible under high contrast. Overdensity estimates are

**Table 2**  
Summary

Field	Redshift	R.A.	Decl.	Galaxies Measured	Overdensity	Peak Surface Density (arcmin <sup>-2</sup> )
CL J0442+0202	$z = 1.10$	4:42:23.7	+02:02:20	48	$19.2\sigma$	42.4
3C 068.2	$z = 1.57$	2:34:23.8	+31:34:17	31	$14.4\sigma$	35.4
MS 1426.9+1052	$z = 1.83$	14:29:24.1	+10:39:15	33	$12.5\sigma$	32.4

**Note.** Summary table for the three selected candidate clusters. All radio-loud sources have significant galaxy overdensities surrounding them with respect to the NIR field counts provided by Hall & Green (1998). The surface density (in galaxies arcmin<sup>-2</sup>) is measured within the same area as the overdensity for sources  $K_s < 20.5$ .

made using a conservative limiting magnitude in the  $K_s$  frame, well below the detection threshold.

After the photometric solution was applied to the candidate cluster galaxies, a color–magnitude relation (CMR) was constructed using 4" diameter apertures. The aperture size was determined by building a curve of growth for the samples and examining the source light profiles with IMEXAM. The 4" diameter apertures were found to be a suitable balance of light collected versus noise levels.

### 3. CLUSTER-CANDIDATE GALAXY OVERDENSITIES

The most basic technique of identifying clusters is by finding overdensities of galaxies with respect to field counts. The lack of a large overdensity, conversely, does not imply that no cluster exists, as cluster richness and the system's mass were not found to be strongly correlated (Planck Collaboration et al. 2013b), although other recent results have suggested the opposite (Rozo & Rykoff 2014). Following the example of Hall & Green (1998) and Hall et al. (2001), counts of galaxies brighter than  $K_s = 20.5$  surrounding radio-loud quasars consistently show overdensities relative to field counts ( $13.7 \pm 1.5$  arcmin<sup>-2</sup>). Listed in Table 2 is each radio source, its position and redshift, and number of galaxies identified within  $\sim 1'$  of the radio source.

For each cluster candidate, a peak overdensity was determined by counting galaxies with  $K_s < 20.5$  around the radio source, and comparing this to the expected field counts. The difference between the counted and expected (in units of  $\sigma = 1.5$  counts arcmin<sup>-2</sup>) are presented in Table 2 as the galaxy overdensity. The peak surface density for each candidate is computed as the number of galaxies divided by the same area as the peak overdensity, written in units of galaxies per square arcminute.

The lowest redshift source in this sample was found to have the largest overdensity of  $19.2\sigma$  above the mean value, followed by 3C 068.2 with a  $14.4\sigma$  overdensity. The greatest redshift candidate cluster (at  $z=1.83$ ) around MS 1426.9+1052 had the smallest overdensity of  $12.6\sigma$ . This can be attributed to the off-center position of MS 1426.9+1052 in the SQUID image (see Figure 5), effectively limiting the potential number of galaxies, coupled with the smaller amount of time the cluster candidate has had to dynamically assemble ( $\sim 2$  Gyr between  $z = 1.11 \rightarrow 1.83$ ).

The expected number of field galaxies that reside within the region associated with each overdensity can be estimated utilizing the counts of Hall & Green (1998). Within the areas associated with the peak overdensities (e.g.,  $>10\sigma$ ), the estimated number of galaxies unassociated with the cluster is  $\sim 4/13$ ,  $\sim 4/10$ , and  $\sim 4/10$  for CL J0442+0202, 3C 068.2, and MS 1426.9+1052, respectively. As each cluster candidate's overdensity is contained within approximately the same area on

the sky, they have approximately the same number of expected field galaxies.

It is important to note that galaxies which exist outside of the largest overdensity can still be associated with the cluster. For instance, out of the six spectroscopically confirmed members within CL J0442+0202, Galaxy 4 in Table 3 is in an area outside an even modest overdensity ( $<3\sigma$ ). Within the cluster discovered by Papovich et al. (2010) at  $z = 1.62$ , 8 of the 11 spectroscopically confirmed members would exist outside of a  $\sim 1\sigma$  overdense region if these galaxies were inserted into our data. This suggests that at these redshifts, clusters are still in the process of assembly with galaxies infalling.

By computing the expected number of galaxies for a projected area in square arcseconds around the radio source, an overdensity factor can also be computed. The inner regions show a factor of  $\sim 11.6$ ,  $6.9$ , and  $6.1$  times the expected number of galaxies near CL J0442+0202, 3C 068.2, and MS 1426.9+1052, respectively. These overdensities indicate that the three regions are candidates for clusters in the process of assembly.

## 4. CLUSTER CANDIDATES

### 4.1. CL J0442+0202

Stern et al. (2003) discovered a NIR galaxy overdensity surrounding the radio source MG1 J04426+0202 at a redshift of  $z = 1.11$ , and did follow-up observations spectroscopically and in the X-ray with *Chandra*. Five other galaxies were spectroscopically confirmed to be cluster members, and a number of X-ray point sources were resolved. However, Stern et al. (2003) were not able to detect diffuse X-ray emission from the ICM, only from the central radio source and other point sources. The NIR photometry of the cluster was measured in the *I*-band and Lick  $K'$  to a limiting magnitude of  $K' < 20$ .

We present SQUID photometry to a deeper limiting magnitude of  $K_s < 20.5$ . A comparison of 10 galaxies with  $K' < 19.1$  mag in the sample of Stern et al. (2003) with ours reveals a systematic offset of  $K' - K_s = 0.32 \pm 0.16$  mag. This provides a basic check of the photometric solution for the SQUID camera, as well as a comparison to published work. The offset could be at least partially attributed to the blueward shift of the  $K'$  filter. The uncertainty in the offset approximately mirrors the uncertainty within our own photometry, while the uncertainty of the  $K'$  photometry from Stern et al. (2003) is unknown.

Within the FOV (shown in Figure 1), we present the photometry of 48 galaxies in Table 3 and the resulting CMR in Figure 2. Spectroscopically confirmed members (Stern et al. 2003) are consistent with being on a red sequence (RS), which may indicate the initial establishment of the prominent RSs of early-type galaxies common in rich, low-redshift clusters (e.g., Coma; Eisenhardt et al. 2007). There is

**Table 3**  
CL J0442 Sources

Galaxy	$\Delta$ R.A. (")	$\Delta$ Decl. (")	$\Delta r$ (")	$K_s$ (mag)	$J - K_s$ (mag)
1	0.000	0.000	0.000	$17.06 \pm 0.19$	$1.73 \pm 0.21$
2	27.571	-37.814	46.798	$18.11 \pm 0.20$	$1.52 \pm 0.22$
3 <sup>b</sup>	42.527	-17.161	45.859	$17.95 \pm 0.20$	$2.15 \pm 0.23$
4 <sup>a</sup>	28.336	-15.598	32.345	$18.67 \pm 0.20$	$1.73 \pm 0.24$
5	4.610	-13.686	14.441	$20.70 \pm 0.49$	$0.79 \pm 0.58$
6 <sup>c</sup>	-9.483	-11.521	14.922	$18.12 \pm 0.20$	$1.30 \pm 0.22$
7 <sup>b</sup>	-23.240	-9.315	25.037	$17.59 \pm 0.19$	$1.73 \pm 0.21$
8	6.097	-7.555	9.709	$17.75 \pm 0.19$	$0.88 \pm 0.21$
9	23.292	-3.630	23.574	$18.80 \pm 0.21$	$1.25 \pm 0.23$
10	-0.907	4.254	4.350	$19.54 \pm 0.26$	$1.74 \pm 0.37$
11 <sup>a</sup>	-7.788	5.418	9.487	$18.11 \pm 0.20$	$1.63 \pm 0.22$
12 <sup>c</sup>	-2.979	11.825	12.194	$19.17 \pm 0.22$	$0.86 \pm 0.25$
13	13.204	14.311	19.472	$18.50 \pm 0.20$	$1.63 \pm 0.23$
14 <sup>a</sup>	3.693	14.121	14.596	$19.20 \pm 0.22$	$1.59 \pm 0.28$
15	-28.050	29.989	41.063	$19.07 \pm 0.21$	$1.59 \pm 0.26$
16	-21.010	-46.483	51.011	$19.51 \pm 0.25$	$0.72 \pm 0.28$
17	15.502	34.860	38.151	$19.30 \pm 0.23$	$1.97 \pm 0.33$
18 <sup>b</sup>	17.970	40.284	44.111	$18.38 \pm 0.20$	$1.62 \pm 0.23$
19	33.668	28.809	44.311	$19.74 \pm 0.26$	$1.93 \pm 0.40$
20	-12.425	-8.076	14.819	$19.53 \pm 0.23$	$1.95 \pm 0.38$
21	-8.792	0.011	8.792	$20.16 \pm 0.41$	$1.39 \pm 0.58$
22	-31.158	-2.055	31.226	$20.04 \pm 0.30$	$0.73 \pm 0.34$
23	-33.491	1.069	33.508	$19.62 \pm 0.25$	$1.17 \pm 0.30$
24	-11.603	-34.214	36.128	$19.25 \pm 0.22$	$1.86 \pm 0.31$
25	-32.993	-37.985	50.313	$18.05 \pm 0.20$	$0.72 \pm 0.21$
26	-15.997	-49.336	51.865	$19.34 \pm 0.23$	$1.38 \pm 0.28$
27	66.671	-35.440	75.505	$18.99 \pm 0.21$	$1.08 \pm 0.24$
28 <sup>a</sup>	4.659	23.257	23.719	$19.12 \pm 0.22$	$1.82 \pm 0.29$
29	-6.299	26.279	27.024	$19.10 \pm 0.21$	$1.89 \pm 0.28$
30	20.863	29.580	36.197	$19.92 \pm 0.30$	$0.91 \pm 0.34$
31	36.724	19.865	41.752	$20.09 \pm 0.31$	$1.47 \pm 0.43$
32	11.888	-43.960	45.539	$19.24 \pm 0.22$	$1.72 \pm 0.31$
33	56.662	20.766	60.347	$19.67 \pm 0.27$	$0.99 \pm 0.31$
34	40.150	49.944	64.082	$20.14 \pm 0.34$	$0.85 \pm 0.40$
35	43.020	55.760	70.426	$19.22 \pm 0.23$	$1.13 \pm 0.26$
36	23.452	56.852	61.500	$19.18 \pm 0.22$	$1.45 \pm 0.27$
37	51.838	50.321	72.245	$18.54 \pm 0.20$	$2.58 \pm 0.30$
38	25.158	-0.324	25.160	$19.53 \pm 0.24$	$1.59 \pm 0.32$
39 <sup>c</sup>	7.734	52.856	53.419	$18.55 \pm 0.20$	$1.71 \pm 0.24$
40	14.390	38.199	40.820	$20.47 \pm 0.38$	$0.87 \pm 0.44$
41	68.910	39.558	79.457	$19.06 \pm 0.22$	$2.02 \pm 0.33$
42	42.107	48.183	63.989	$19.64 \pm 0.25$	$1.49 \pm 0.33$
43	23.571	26.444	35.424	$20.29 \pm 0.34$	$0.84 \pm 0.40$
44	32.678	10.572	34.346	$19.87 \pm 0.27$	$2.35 \pm 0.60$
45	-29.289	13.467	32.236	$19.49 \pm 0.24$	$2.20 \pm 0.41$
46	-27.731	-15.182	31.615	$20.02 \pm 0.30$	$1.90 \pm 0.52$
47	25.050	-16.000	29.724	$19.86 \pm 0.27$	$1.31 \pm 0.35$
48 <sup>a</sup>	-2.0272	-2.370	3.118	$18.43 \pm 0.20$	$1.76 \pm 0.24$

**Notes.** The central radio source MG1 J04426+0202 (Galaxy 1) and the sources around it within the SQUID field. Galaxy 1 is located at R.A. = 4:42:23.7 Decl. = +02:02:20 with separations ( $\Delta$ R.A.,  $\Delta$ Decl.) computed with respect to it.

<sup>a</sup> Spectroscopically confirmed cluster members (Stern et al. 2003).

<sup>b</sup> Non-members in the field (Stern et al. 2003).

<sup>c</sup> X-ray point sources found with *Chandra* that are not cluster members (Stern et al. 2003).

also a bright interloper ( $K_s = 17.59$ ) posing as an RS member. There are also foreground and background AGNs (bright X-ray point sources found with *Chandra*) that are entangled within the CMR. The overdensity remains significant, but the

aforementioned interlopers urge caution in relying on purely photometric results.

#### 4.2. 3C 068.2

The photometry for the galaxies around 3C 068.2 is in Table 4. Within  $\sim 1$  arcmin of the central radio source (Galaxy 1 in the table), which corresponds to roughly  $\sim 0.5$  Mpc in the assumed cosmology (Wright 2006), 31 extended sources were identified. The selected sources are shown in Figure 3.

A  $K_s$ ,  $J - K_s$  CMR of the sources is in Figure 4, displaying a flat RS of  $J - K_s \approx 2$ . The two bright galaxies on the RS with  $K_s = 16.30$ ,  $17.55$  likely contain AGNs, as they were identified as X-ray point sources by Wilkes et al. (2013) with *Chandra*.

It is interesting to note that the central 3C source in this case is neither on the RS, nor is it the brightest cluster galaxy. Instead, it is found in the so-called blue cloud, inhabited primarily by star-forming galaxies. Barthel et al. (2012) surveyed a number of 3C sources with *Herschel* and integrated the far-infrared dust emission to calculate the star-formation rate (SFR) of each galaxy. 3C 068.2 has a calculated SFR of  $\sim 390 M_\odot \text{yr}^{-1}$ . This exceptionally high SFR cannot be sustained for a Hubble time without exceeding the total mass of the largest known galaxies. This might suggest that this galaxy has been caught in the act of formation prior to its transition from the blue cloud to the RS.

#### 4.3. MS 1426.9+1052

MS 1426 is the most distant candidate cluster in this sample, and it contains a large number of potential cluster galaxies, with 34 measured photometrically in Table 5. The SQUID image (Figure 5) surrounding the radio source was slightly off-center, so the selected galaxies are not evenly distributed from the radio source. The CMR is shown in Figure 6, with an RS color consistent with the CMRs for CL J0442+0202 (Figure 2) and surrounding 3C 068.2 (Figure 4).

Richards et al. (2009) computed photometric redshifts of regions surrounding radio-loud sources within the SDSS database. There are two galaxies near MS 1426.9+1052 with photometric redshifts of  $z = 1.83$ , but were unfortunately off of the edge of the SQUID image. However, this provides a further indication that the field hosts a possible structure, in addition to the presence of an RS in the CMR and the associated galaxy overdensity that was discussed in Section 3.

## 5. DISCUSSION

Perhaps one of the oldest galaxy correlations is the one between galaxy absolute luminosity and global color, the CMR (i.e., the CMR; Baum 1959; Faber 1973; Visvanathan & Sandage 1977). The CMR has been demonstrated to exist from the near-UV (Kaviraj et al. 2007) to NIR wavelengths (Chang et al. 2006). A majority of these CMR studies can be summarized such that (1) the correlation is one of redder galaxy colors with increasing galaxy luminosity, (2) the correlation exists over a range of galaxy environments, but is strongest in the densest galaxy regions (Cooper et al. 2008), and (3) there exist distinct red and blue components to the CMR, with the red component being composed of early-type galaxies (ellipticals and S0's, see Bower et al. 1992; van Dokkum et al. 1998; Baldry et al. 2004; Bell et al. 2004; Hogg et al. 2004; López-Cruz et al. 2004; Bernardi et al. 2005;

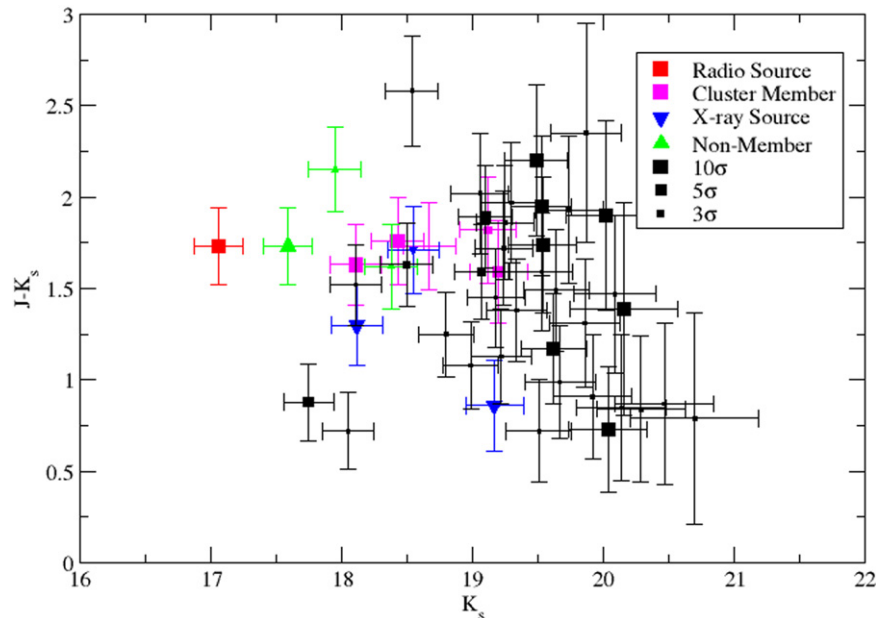


**Figure 2.** Radio-loud source (MG1 J04426+0202) at the center of CL J0442+0202 is shown by a red square as the brightest cluster galaxy (BCG), and is also a part of the red sequence ( $J - K_s = 1.73$ ) in this color–magnitude diagram. The next brightest galaxy along the red sequence (a green triangle at  $K_s = 17.59$ ,  $J - K_s = 1.73$ ) is a spectroscopically confirmed interloper. Magenta squares are confirmed members (Stern et al. 2003), while foreground/background X-ray emitting AGNs are represented by blue downward triangles. Galaxies that are found within the region corresponding to at least a  $10\sigma$  galaxy overdensity have the largest symbols, while the smallest points correspond to galaxies located in a region with an overdensity  $<3\sigma$ . Within the largest overdensity region, approximately four sources are expected to be unassociated with the cluster.

McIntosh et al. 2005; de Lucia et al. 2006; Gallazzi et al. 2006).

The CMR is a member of a number of fundamental relations that relate the global properties in early-type galaxies, such as mass and kinematics (Dressler et al. 1987). Various formation and evolutionary scenarios are proposed to explain these fundamental relationships (Gavazzi et al. 1996). For example, galaxy interactions can remove the gas used for star formation and produce a relationship between age and galaxy mass (Moore et al. 1999). Ram pressure stripping can also strip galactic gas and halt star formation (Tecce et al. 2010). However, the comparison between spectroscopic indices and galaxy color indicates that the CMR is most strongly linked to the chemical enrichment history of a galaxy, as redder colors map directly into increasing metallicities (Bernardi et al. 2005; Thomas et al. 2005). The slope and scatter of the CMR can be reproduced if the redshift of galaxy formation is greater than 5 (Bower et al. 1998) even with a small amount of mass growth by mergers or bluer colors with recent star formation.

With respect to cluster populations, the CMR has also been used to define the “red envelope” or RS (Ellis & Fabian 1988), the boundary between old, quiescent galaxies and star-forming systems. The small amount of scatter for the RS of the CMR has been used to argue that early-type galaxies are coeval and have evolved passively since their formation epoch (McIntosh et al. 2005; Schombert & Rakos 2009b). The blue population (the “blue cloud”) can be compared to the red population by assigning the fraction of galaxies below 0.2 mag of the RS; this fraction ( $f_B$ ) becomes an indicator of the global star-formation history in cluster populations. It can also be followed as a function of redshift (the Butcher–Oemler effect; Butcher & Oemler 1984), a key parameter for numerous galaxy formation and evolution scenarios.

The examination of the CMR in our sample begins with the construction of a fiducial CMR based on a sample of 1104 ellipticals in the local universe (Schombert & Rakos 2009b). The midline to that CMR, based on narrow band colors between 4100 and 5500 Å, is well described by the 12 Gyr old multi-metallicity models constructed in Schombert & Rakos (2009a). These models adopt the spectral energy distribution (SED) spectra from Bruzual & Charlot (2003) for single metallicity and age populations and convolve each age/metallicity with a star formation history (initial burst) and chemical enrichment scenario as outlined in Schombert & Rakos (2009a). The result is a perfect match to the optical CMR using only old (12 Gyr) populations of varying metallicity. Interpretations of the CMR implying the need for younger stars (frosting models; see Trager et al. 2000) appear to be the consequence of neglecting the old, metal-poor (i.e., blue) component of the metallicity distribution (Schombert & Rakos 2009a). This has been independently confirmed by Bregman et al. (2006) analyzing the infrared SEDs of early-type galaxies.

The CMR defined by optical colors is not directly transferable to this project, as the  $JK$  observations for this sample do not use redshifted filter sets as employed by the Rakos & Schombert program. Thus, we must convolve the  $JK$  bandpasses to the rest-frame model spectra. The three cluster redshifts (1.10, 1.57, 1.83) place the center of the  $J$  filter at rest frames 6000, 4903, 4452 Å, and the  $K$  filter at 10571, 8775, 7845 Å, respectively. This places the observed colors between the Johnson  $B$  and  $I$  range, redward of the 4000 Å break. As the typical elliptical has a spectral intensity peak at 4600 Å (before a sharp drop off at the 4000 Å break and the metal line rich region between 4200 and 4800 Å), our expectation is that the observed  $J - K$  colors will increase (redden) from  $z = 1.10$  to 1.57, then shift blueward at  $z = 1.83$

**Table 4**  
3C 068.2 Sources

Galaxy	$\Delta R.A.$ (")	$\Delta Decl.$ (")	$\Delta r$ (")	$K_s$ (mag)	$J - K_s$ (mag)
1	0.000	0.000	0.000	$18.33 \pm 0.17$	$1.60 \pm 0.24$
2	-13.247	39.826	41.971	$18.61 \pm 0.19$	$1.19 \pm 0.24$
3	4.572	34.854	35.153	$17.94 \pm 0.15$	$1.93 \pm 0.21$
4 <sup>a</sup>	-7.548	27.028	28.063	$16.30 \pm 0.10$	$1.99 \pm 0.13$
5 <sup>a</sup>	-12.031	21.261	24.429	$17.55 \pm 0.13$	$2.09 \pm 0.19$
6	31.568	20.292	37.528	$19.26 \pm 0.25$	$0.92 \pm 0.32$
7	53.111	5.645	53.410	$18.84 \pm 0.21$	$0.94 \pm 0.26$
8	-14.288	0.963	14.321	$18.68 \pm 0.19$	$0.78 \pm 0.23$
9	-46.977	-6.956	47.489	$18.34 \pm 0.17$	$0.98 \pm 0.21$
10	-12.658	-13.683	18.640	$18.84 \pm 0.21$	$1.04 \pm 0.26$
11	12.944	-43.318	45.211	$19.28 \pm 0.25$	$1.42 \pm 0.35$
12	-1.630	-20.314	20.379	$19.42 \pm 0.27$	$1.89 \pm 0.43$
13	16.984	-29.481	34.023	$20.17 \pm 0.40$	$0.59 \pm 0.47$
14	12.224	4.321	12.966	$19.98 \pm 0.38$	$4.06 \pm 2.14$
15	-0.121	-8.203	8.204	$19.41 \pm 0.29$	$2.94 \pm 0.80$
16	-6.447	1.032	6.529	$19.67 \pm 0.32$	$2.28 \pm 0.61$
17	20.055	-23.083	30.578	$19.67 \pm 0.32$	$2.64 \pm 0.69$
18	-22.220	-25.015	33.459	$20.02 \pm 0.38$	$3.30 \pm 1.25$
19	-30.541	-30.224	42.968	$19.76 \pm 0.31$	$0.52 \pm 0.37$
20	28.521	-41.641	50.472	$19.99 \pm 0.37$	$1.62 \pm 0.55$
21	35.474	-39.058	52.763	$20.89 \pm 0.64$	$2.10 \pm 1.21$
22	52.244	-32.845	61.710	$19.99 \pm 0.36$	$0.99 \pm 0.46$
23	19.391	4.007	19.801	$19.91 \pm 0.35$	$1.50 \pm 0.50$
24	14.409	-18.372	23.348	$19.23 \pm 0.26$	$1.63 \pm 0.36$
25	-13.351	-20.148	24.170	$19.38 \pm 0.27$	$1.96 \pm 0.43$
26	28.742	-4.167	29.043	$19.28 \pm 0.26$	$3.67 \pm 0.90$
27	22.496	24.888	33.549	$19.28 \pm 0.26$	$2.36 \pm 0.47$
28	0.204	22.287	22.288	$18.95 \pm 0.22$	$2.48 \pm 0.41$
29	25.898	-2.416	26.010	$19.37 \pm 0.27$	$2.15 \pm 0.45$
30	19.655	23.165	30.380	$19.58 \pm 0.30$	$2.24 \pm 0.53$
31	26.082	-34.725	43.430	$18.74 \pm 0.20$	$1.93 \pm 0.31$

**Notes.** Galaxy candidates within  $\sim 1'$ , which corresponds to  $\sim 0.5$  Mpc at this redshift (Wright 2006), around 3C 068.2 (Galaxy 1) located at R. A. = 2:34:23.8, Decl. = +31:34:17.

<sup>a</sup> X-ray point source identified with *Chandra* (Wilkes et al. 2013).

as the  $J$  filter passes over the 4600 Å bump, as seen in Figure 7 for both a young and old galaxy. Indeed, that is what is seen in the mean cluster colors of  $J - K_s = 1.47 \pm 0.04$  (CL J0442+0202),  $J - K_s = 1.59 \pm 0.06$  (3C 068.2) and  $J - K_s = 1.46 \pm 0.06$  (MS 1426.9+1052), which is the uncertainty-weighted mean of all candidate galaxies.

Comparison to the 12 Gyr old model CMR of Schombert & Rakos (2009b) is made by redshifting the model spectra to the redshift of the sample clusters. The result is shown in Figure 8 (red lines). These CMRs typically lie redward of the observed colors. This is, of course, due to the fact that the model CMR is produced for 12 Gyr populations. The age of the universe at the redshifts of the clusters will be  $\sim 5.5$ , 4 and 3.5 Gyr, respectively.

Altering the CMR for age simply requires recalculating the population model by halting at a younger age. The only color changes are due to age effects (shifts in the turnoff point to the blue) as metallicity effects are minor since single burst models have a rapid enrichment scenario (e.g., the typical early-type galaxy reaches 90% final metallicity in 3 Gyr due to the rapid onset of galactic winds). Recalculating the models (and chemical enrichment) to those cluster ages produces the blue CMR lines in Figure 8. While the correction due to age is relatively small, the age-corrected CMRs are in better

agreement with the cluster data. The close match between the RS and the model CMRs suggests that these rich cluster ellipticals are effectively coeval with an early formation epoch.

The formation redshifts of these cluster candidates are difficult to constrain within the resolution of our data. For instance, using  $z_f = 5$  within our simulations produces RSs that are offset from the blue lines in Figure 8 by  $\Delta(J - K_s) = -0.08, -0.09, -0.12$  for redshifts of  $z = 1.1, 1.57, 1.83$ , respectively. As discussed in Section 4, the  $K'$  photometry of 10 galaxies in CL J0442+0202 from Stern et al. (2003) shows a bias when compared to our  $K_s$  photometry of  $K' - K_s = 0.32 \pm 0.16$ . For these 10 galaxies, this bias could imply a bluer stellar population and thus a smaller  $z_f$ . Within the uncertainties of our data, we cannot formally fit a  $z_f$  to the cluster candidates, but the early-type galaxies are consistent with  $z_f \gtrsim 5$ .

Constraining the formation age of the galaxy in high redshift is challenging because of the inverse relation between redshift and cosmic age. For example, Eisenhardt et al. (2008) found that for a sample of IRAC-selected clusters at redshifts  $z > 1$ ,  $I - [3.6]$  colors favored  $z_f > 3$ , but could also be consistent with  $z_f = 30$  (see their Figure 19) with significant scatter in clusters at redshifts above  $z > 1.5$ . Our results are consistent, with at least a few galaxies appearing on the RS as old populations for their redshift.

Absolute  $M_{5500}$  AB magnitudes were computed by convolving the redshifted  $J$  filter that each cluster is observed in with  $V$ . As illustrated in Figure 7, the filters are compressed at higher redshift, which lowers the flux through the filter, so a  $K$ -correction of  $-0.23, -0.50$ , and  $-0.75$  mag was applied to CL J0442+0202, 3C 068.2, and MS 1426.9+1052, respectively.

Clear, early evidence of evolution in the stellar populations of cluster galaxies is the Butcher-Oemler effect (Butcher & Oemler 1984). Simply stated, the Butcher-Oemler effect is a sharp increase in the fraction of blue galaxies in a cluster as a function of redshift. Rakos & Schombert (1995) studied 509 galaxies in 17 clusters between redshifts of 0 and 1, and found a linearly increasing  $f_B$  from a present-day value of 5% to 80% at a redshift of 1. That study utilized Strömgren photometry to determine a color separation between nearby star-forming galaxies and ellipticals (anything blueward of  $b_z - y_z = 0.20$  or  $v_z - y_z = 0.40$ ), and then used customized filter sets to match those rest frame colors at the respective redshifts of each cluster. Any source bluer than this color separation is considered a member of the blue fraction of the cluster.

To calculate the blue fraction using  $J, K_s$  filters, we computed the probability distribution for the color of each galaxy, and the fraction that falls 0.2 mag bluer than the  $z_f = 10$  CMR models of the RS (blue lines in Figure 8) are considered to be blue galaxies. The 0.2 mag offset is adopted from the example of Butcher & Oemler (1984), and we assumed Gaussian errors for the probability distribution. This results in  $f_B$  values of  $40\% \pm 14\%$  in CL J0442+0202,  $41\% \pm 18\%$  for 3C 068.2, and  $49\% \pm 17\%$  within MS 1426.9+1052. The  $f_B$  are minimally reduced ( $\sim 5\%$ ) if the blue fraction is simply defined as the number of galaxies that are 0.2 mag bluer than the  $z_f = 10$  CMR models. Errors are based on an assumed Poisson distribution ( $\sqrt{N_{\text{obj}}}$ ), as in Rakos & Schombert (1995). A summary of the  $f_B$  values can be found in Table 6.

The  $f_B$  values are less than expected from the rapid increase in  $f_B$  from Rakos & Schombert (1995; see their Figure 4). However, this can be interpreted as a consequence of the cosmic SFR as a function of redshift, in which galaxies at  $z > 1$

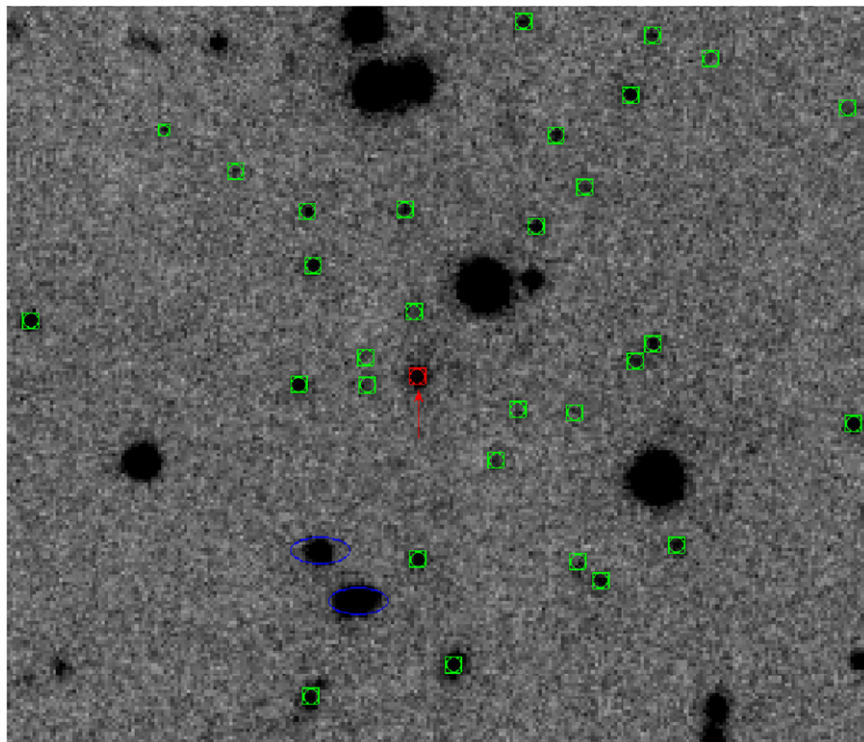


**Figure 3.** NEWFIRM view of sources (green boxes) within  $\sim 1'$  of 3C 068.2. The radio source is indicated by a red arrow and red square. The blue ellipses are X-ray point sources found with *Chandra* (Wilkes et al. 2013).

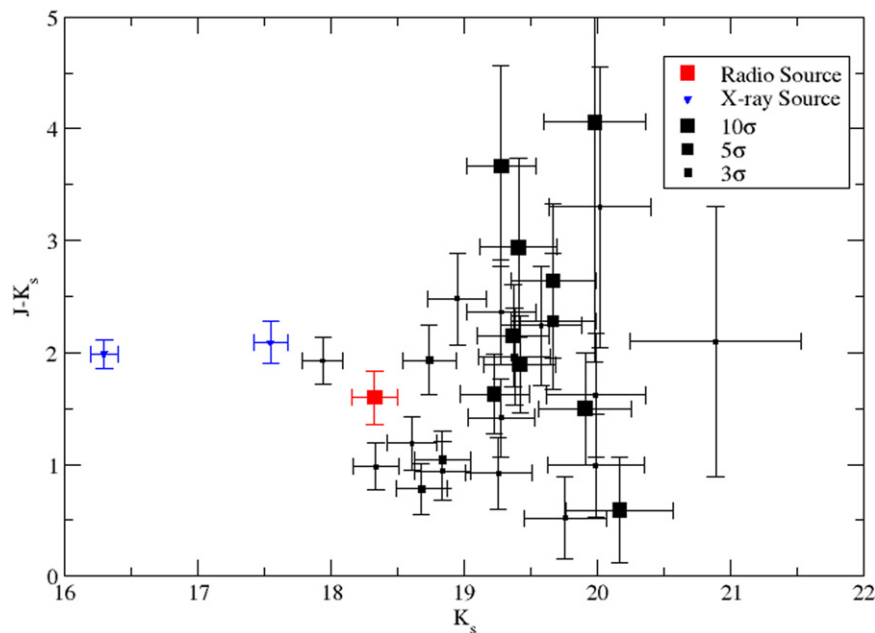


**Figure 4.** Color–magnitude diagram of galaxy sources surrounding 3C 068.2, which is represented by a red square. The radio source is not the brightest cluster galaxy, being located within the blue cloud with a measured star-formation rate of  $\sim 390 M_{\odot} \text{ yr}^{-1}$  (Barthel et al. 2012). The blue, downward triangles are *Chandra* point sources (Wilkes et al. 2013), and are the two brightest galaxies on the flat red sequence ( $J - K_s \sim 2$ ). The larger the size of the symbol, the more significant the overdensity the galaxy resides in. The largest symbol corresponds to a galaxy within the area corresponding to at least a  $10\sigma$  overdensity. Within this region,  $\sim 4$  galaxies are expected to be unassociated with the cluster.

have nearly constant SFR (Madau et al. 1996), while the rate steadily declines from  $z = 1 \rightarrow 0$ . Updated versions of the Madau diagram confirm this trend out to  $z \sim 3$  (Pérez-González et al. 2005). Our values of the blue fraction also agree with the more intensive spectroscopic GMASS study (Cassata et al. 2008) which finds  $f_B$  of 50% at redshifts of 2.

Indeed, Newman et al. (2014) find a cluster at  $z = 1.8$  that hosts 15/19 spectroscopically confirmed, quiescent members, further corroborating blue fractions that are sometimes small at this epoch. These differences could point to large variations in stages of cluster assembly and evolution in the universe at these high redshifts.

**Table 5**  
MS 1426 Sources

Galaxy	$\Delta$ R.A. ( $''$ )	$\Delta$ Decl. ( $''$ )	$\Delta r$ ( $''$ )	$K_s$ (mag)	$J - K_s$ (mag)
1	0.000	0.000	0.000	$17.32 \pm 0.18$	$1.65 \pm 0.28$
2	-40.712	-35.650	54.115	$19.25 \pm 0.22$	$0.87 \pm 0.31$
3	-51.641	-29.798	59.622	$18.53 \pm 0.19$	$1.53 \pm 0.29$
4	-24.161	-28.263	37.183	$18.74 \pm 0.20$	$2.27 \pm 0.33$
5	-27.625	-29.245	40.229	$17.94 \pm 0.18$	$1.81 \pm 0.29$
6	-2.455	-22.960	23.091	$19.32 \pm 0.23$	$1.86 \pm 0.36$
7	-4.699	-14.326	15.077	$19.32 \pm 0.23$	$1.19 \pm 0.34$
8	-1.657	-8.484	8.645	$17.86 \pm 0.18$	$1.89 \pm 0.29$
9	18.830	-7.844	20.398	$18.52 \pm 0.19$	$1.11 \pm 0.29$
10	10.365	-4.190	11.180	$18.31 \pm 0.19$	$0.56 \pm 0.28$
11 <sup>a</sup>	-17.572	1.746	17.658	$18.88 \pm 0.21$	$0.88 \pm 0.30$
12	18.403	4.213	18.879	$18.98 \pm 0.20$	$1.06 \pm 0.30$
13	-18.602	5.316	19.347	$17.98 \pm 0.19$	$0.82 \pm 0.28$
14	-6.800	7.373	10.030	$18.28 \pm 0.19$	$1.74 \pm 0.29$
15	31.851	8.302	32.915	$16.84 \pm 0.18$	$1.63 \pm 0.28$
16	3.553	14.216	14.653	$18.10 \pm 0.19$	$1.62 \pm 0.29$
17	16.026	21.328	26.678	$18.36 \pm 0.19$	$1.24 \pm 0.29$
18	20.009	33.412	38.945	$18.95 \pm 0.21$	$1.54 \pm 0.32$
19	21.558	7.115	22.702	$20.88 \pm 0.60$	$-0.34 \pm 0.64$
20	0.422	-19.404	19.409	$20.70 \pm 0.54$	$0.33 \pm 0.61$
21	-31.632	2.164	31.706	$19.91 \pm 0.31$	$1.03 \pm 0.40$
22	-3.954	67.597	67.712	$18.65 \pm 0.20$	$1.01 \pm 0.29$
23	-32.659	59.472	67.850	$17.55 \pm 0.18$	$2.31 \pm 0.29$
24	-43.508	65.673	78.777	$17.94 \pm 0.19$	$1.99 \pm 0.29$
25	-36.862	67.383	76.807	$17.14 \pm 0.18$	$1.71 \pm 0.28$
26	-53.406	60.234	80.501	$19.22 \pm 0.23$	$1.52 \pm 0.34$
27	-76.388	0.576	76.390	$18.82 \pm 0.23$	$2.78 \pm 0.78$
28	3.388	48.021	48.140	$19.78 \pm 0.28$	$0.97 \pm 0.37$
29	-51.012	36.668	62.823	$20.21 \pm 0.38$	$0.43 \pm 0.46$
30	14.034	13.015	19.141	$19.44 \pm 0.24$	$2.52 \pm 0.54$
31	12.620	34.705	36.928	$19.43 \pm 0.25$	$2.62 \pm 0.57$
32	-62.294	-16.795	64.518	$19.00 \pm 0.21$	$1.97 \pm 0.34$
33	-44.385	-11.477	45.845	$19.45 \pm 0.27$	$2.11 \pm 0.45$

**Notes.** Galaxies surrounding Galaxy 1 (R.A. = 14:29:24.1 and Decl. = +10:39:15), the radio source MS 1426.9+1052.

<sup>a</sup> Has a measured photometric redshift of  $z = 1.265$  using SDSS data (Richards et al. 2009).

If the sample is restricted to the regions of maximum overdensity within each cluster (e.g.,  $>10\sigma$ , discussed in Section 3), the blue fraction decreases in the two low redshift targets but increases for MS 1426.9+1052. CL J0442+0202 has a relatively minor decrease to  $f_B = 38\% \pm 29\%$ , while 3C 068.2 at  $z = 1.57$  decreases from  $f_B = 41\% \pm 18\% \rightarrow 27^{+33}_{-27}\%$ . MS 1426.9+1052 at  $z = 1.83$  increases its blue fraction within the region of largest overdensity by 11% to  $f_B = 60\% \pm 33\%$ . The large variability between candidate clusters at a range of redshifts is an interesting test of the evolution for cluster galaxies, as the innermost regions should have had the most dynamical interaction.

We also define the faint red fraction of galaxies ( $f_{fr}$ ) as those galaxies that are  $1.5 M_{5500}$  AB magnitudes fainter than the spectroscopically confirmed BCG for each candidate cluster and 0.2 mag redder than the CMR model RS line used to compute the blue fraction, once again using the probability distribution with assumed Gaussian errors for each galaxy. CL J0442+0202 has an  $f_{fr} = 25\% \pm 14\%$  for the entire sample of galaxies measured, and  $f_{fr} = 27^{+29}_{-27}\%$  within the region of  $>10\sigma$  overdensity. At the redshift of  $z = 1.57$ , 3C 068.2 has a

$f_{fr} = 26\% \pm 18\%$  overall, but a 22% increase within the central overdensity to  $f_{fr} = 48\% \pm 33\%$ , which corroborates the results from its  $f_B$  measurement. Our highest redshift candidate MS 1426.9+1052 has a comparatively low red fraction within the overdense region of a mere  $f_{fr} = 10^{+33}_{-10}\%$ , with  $f_{fr} = 24\% \pm 17\%$  for the entire sample. These faint, red galaxies are presumably reactants in future dry mergers that would be hierarchically accreted to form galaxies on the RS. The blue and faint red fractions are listed in Table 6.

Simple scenarios to build up the RS via the quenching and merging of blue galaxies, followed by dry mergers, have been proposed by Faber et al. (2007). These would require a significant population of interacting blue disk galaxies to transform relatively weak CMRs at high redshift into the developed RS features seen in rich, nearby clusters (see Figures 3 and 4 in Eisenhardt et al. 2007). Papovich et al. (2012) conclude that a series of dry mergers is the dominant mechanism in the growth of quiescent galaxies based on an in-depth analysis of a cluster at  $z = 1.62$ . The processes that shape the growth of even the most massive galaxies do not seem to be resolved. Some recent studies conclude that ongoing mergers after  $z \sim 1.5$  are necessary to match the present-day BCGs (Ferreras et al. 2012; Fassbender et al. 2014), while Fritz et al. (2014) suggest that major mergers are of minimal importance.

The extent to which there is a well-defined RS CMR at high redshift impacts our models of galaxy formation. CMRs out to redshifts of 1 are well established (see Mei et al. 2009 and references therein) as well as in some protoclusters at redshifts of up to  $z = 4$  (Steidel et al. 2005; Overzier et al. 2008). The stellar populations of galaxies on the RS at  $z = 1.5$ , which match passively evolving color evolution models, is consistent with the massive, bright end of the CMR being in place by a few Gyr after the dawn of time. This suggests that at least some massive galaxies experience the epoch of primary star formation at quite high redshift. Our results are consistent with the findings of Eisenhardt et al. (2008; see their Figures 17 and 19).

This is in agreement with the observation that protocluster galaxies are, in general, older than field galaxies of the same redshift (Peter et al. 2007), as if high density environments accelerate galaxy color and morphological evolution. Larger intrinsic scatter in the CMR with redshift has been interpreted as due to age effects (Mei et al. 2009); however, it becomes increasingly difficult to separate passive age changes in ellipticals with increasing star formation in the blue cloud. The separation between the RS and the blue cloud becomes problematic inside of 2 Gyr from the onset of galaxy formation.

The RS is nominally identified with ellipticals in the cluster core region, for they have the reddest colors out to high redshifts (Mei et al. 2009). This is supported by the fact that the slope and zeropoint of the CMR is unchanged (aside from age corrections) between our sample (at a mean redshift of 1.5) and the present day. The galaxies producing an increasing blue fraction with redshift are perhaps the cluster proto-S0 population, for they have the largest color scatter in present-day clusters and would match the ‘‘quenching’’ scenario, where infalling galaxies interact with the cluster environment to halt star formation (Rakos & Schombert 1995; Faber et al. 2007).

While the results presented herein are similar to other studies based on spectroscopic and space-imaging morphology, we achieve many of the same goals with respect to the star-

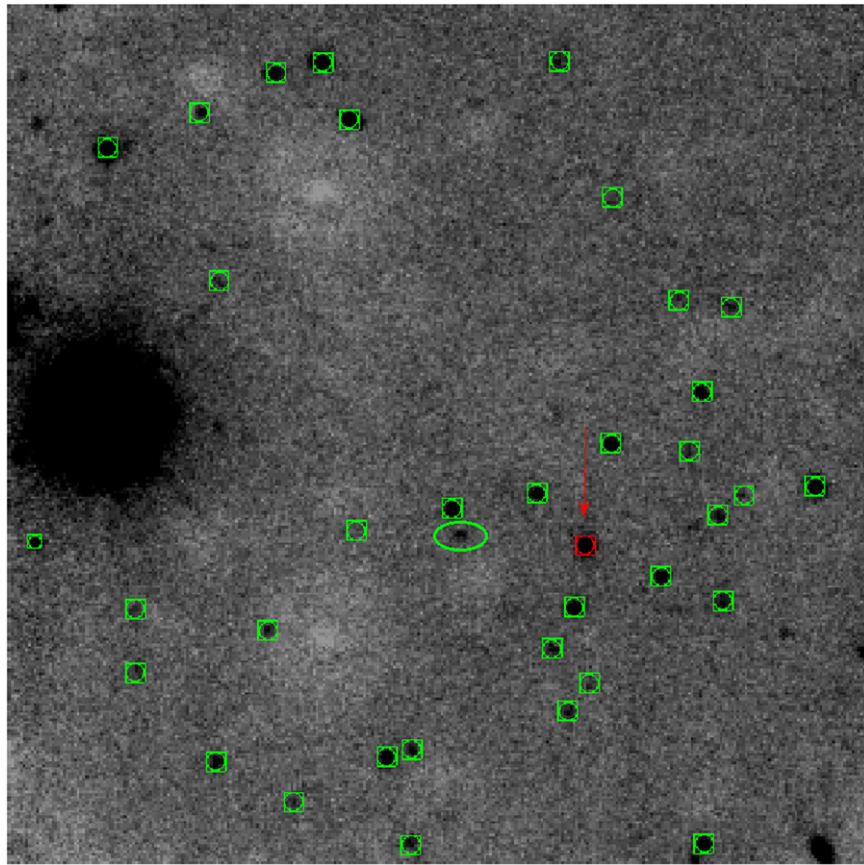


**Figure 5.**  $K_s$  image around MS 1426.9+1052 with the SQUID camera. The large, saturated object on the left-hand side of the image is a  $K_s = 9.17$  mag star in the 2MASS Point Source Catalog. The radio source is indicated by a red arrow and box, while the green ellipse indicates a galaxy with a photometric redshift of  $z = 1.265$  (Richards et al. 2009). The green boxes are the remainder of galaxy sources found within the field. The image size is  $120'' \times 120''$ .

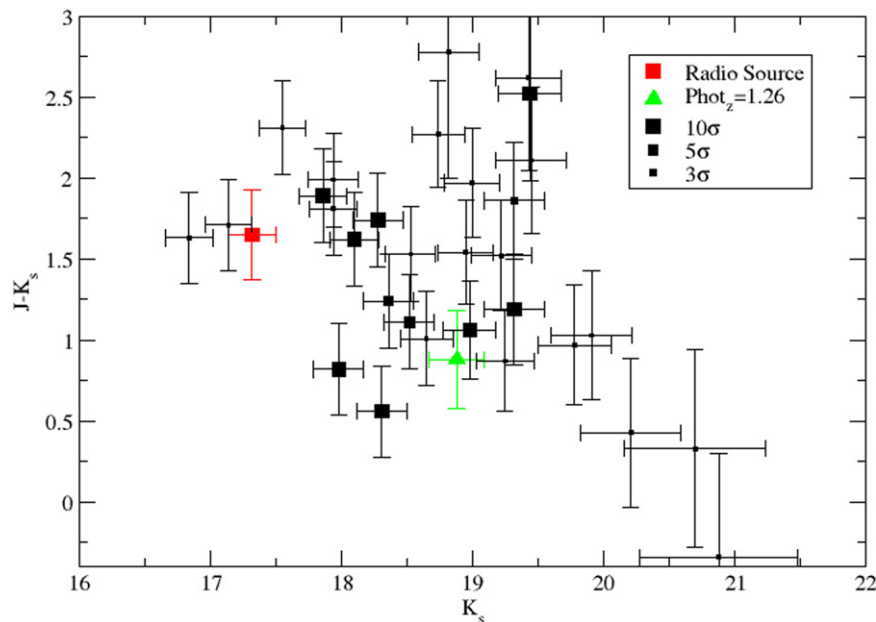


**Figure 6.** Color–magnitude diagram for galaxies surrounding the central radio source (red square). The green upwards triangle is a probable interloping galaxy with a photometric redshift of  $z = 1.265$  (Richards et al. 2009) when compared to the redshift of the radio source at  $z = 1.83$ . The largest symbols represent galaxies found within the area corresponding to a  $10\sigma$  overdensity, of which roughly four are expected to be field galaxies.

formation history of cluster galaxies, but with a much smaller amount of telescope time. In addition, the identification of the high redshift clusters themselves, as preliminary observations

before spectroscopy on large aperture telescopes and limited space-imaging time, argues for an extensive ground-based NIR survey of the environment around radio sources. The analysis

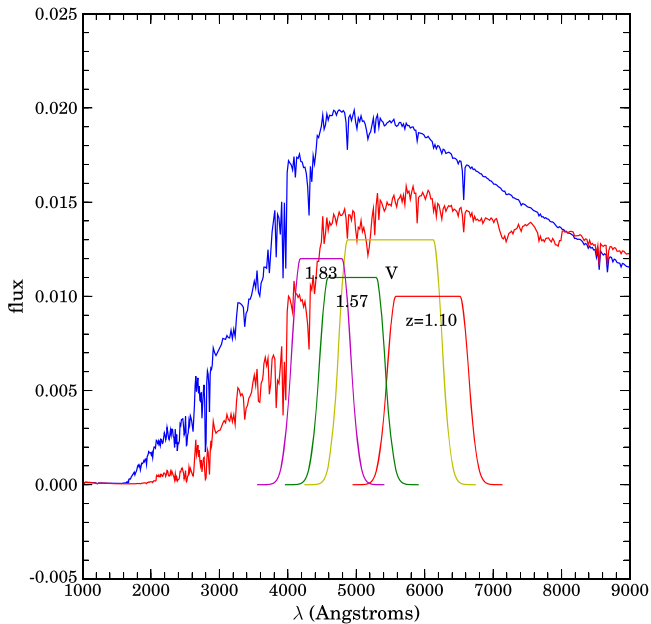


**Figure 7.** Model SED for an old (12 Gyr) galaxy in red, with the blue spectrum illustrating a young galaxy more representative of the expected SED at the high redshift of the cluster candidate galaxies. Overlying the SEDs are the de-redshifted  $J$  filters for each candidate cluster, with  $V$  as a reference. At increasing redshifts, the observed filters narrow and measure less flux, so  $K$ -corrections were applied to the computed  $M_{5500}$  AB magnitudes for each source. Flux is in arbitrary units.

of the photometric CMR, combined with accurate stellar population models, provides a different window into the star formation history of cluster galaxies.

## 6. SUMMARY AND FUTURE WORK

We have presented three candidate galaxy clusters spanning the redshift regime of  $z = 1.10$ – $1.83$  identified as NIR galaxy overdensities surrounding radio-loud sources. From deep NIR imaging, color–magnitude diagrams were constructed and compared to the galaxy models of Schombert & Rakos (2009b). We find that the ellipticals on the RS within each cluster candidate were all formed at a relatively old age. The data are consistent with  $z_f \gtrsim 5$  in our models, but we lack the resolution to formally fit a formation redshift. These apparently old, massive RS galaxies, while clearly present, are a minority of the cluster population. There is a slowly increasing blue fraction of galaxies within each cluster candidate as a function of redshift, from  $f_B = 40\%$  at  $z = 1.11$  up to  $f_B = 48\%$  at  $z = 1.83$ .

The candidate clusters are prime targets for further study. Use of the *Hubble Space Telescope*’s superior imaging capabilities, compared to ground-based NIR images, could provide galaxy morphology and mass estimates (Cassata et al. 2013), along with measurements of individual SFRs (Lee et al. 2014b), even at these redshifts. The two candidates with larger redshifts, 3C 068.2 and MS 1426.9+1052, would benefit from multi-object spectroscopy, primarily to establish cluster membership, while secondarily providing insight into the types of galaxies inhabiting proto-clusters (e.g., emission line signatures), as Stern et al. (2003) did with CL J0442+0202.

In the X-ray, *Chandra* or *XMM-Newton* could potentially be used to confirm these objects as clusters via their ICM emission, as well as providing a mass estimate for the system. Similarly, one could use CARMA to measure the SZ signal,

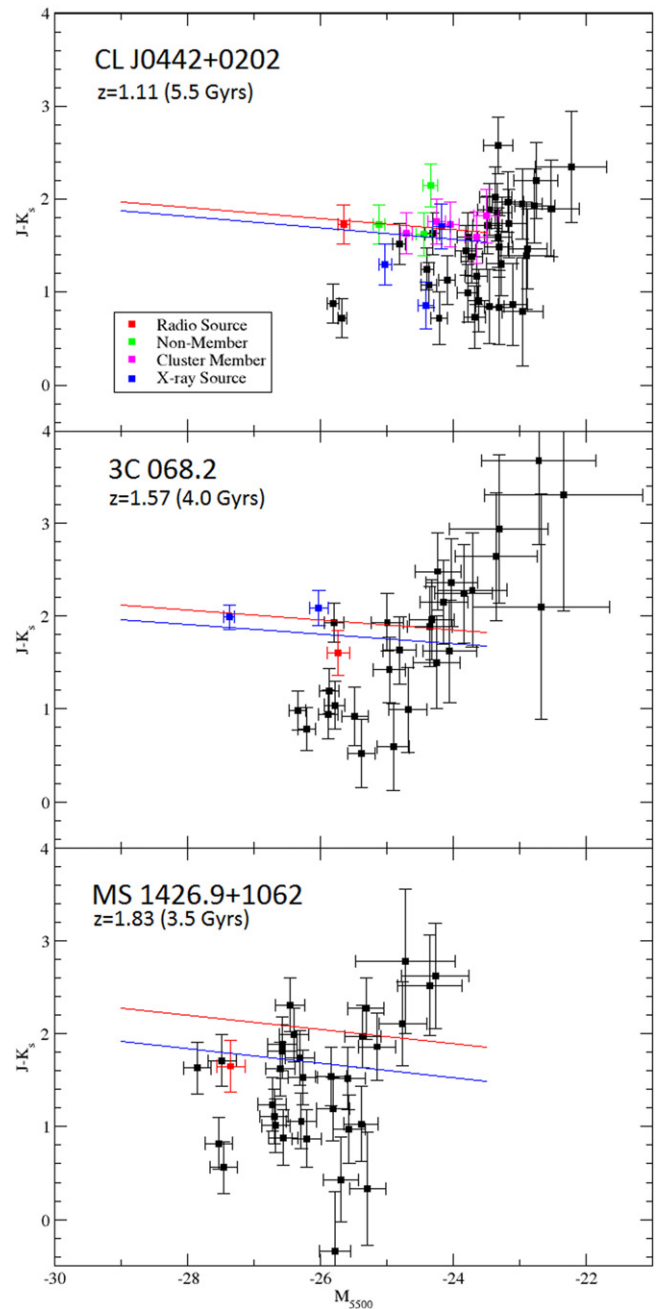


**Figure 8.** Each candidate cluster’s CMR, with absolute  $M_{5500}$  AB magnitudes computed with the assumption that all sources are at the same redshift as the radio-loud source. As in the case of CL J0442+0202, there will be foreground and background interlopers within these CMRs. A  $K$ -correction has been applied to each cluster candidate based on the SED template age and redshift with respect to the  $M_{5500}$  magnitude system (Figure 7). The red CMR line represents the red sequence from the 12 Gyr galaxy models of Schombert & Rakos (2009b), redshifted to the respective value. The blue lines are recomputed SED models for the assumed ages of each candidate cluster, which are listed in the parentheses next to the redshift of the radio source.

which will accomplish similar goals as the aforementioned X-ray observations, but with a potentially more modest investment of telescope time.

Most importantly, a confirmation of the presence of a physical structure with spectroscopic redshifts in any of these potential clusters will add to the small but growing number of high-redshift clusters. The number density as a function of redshift and an estimate of the structure’s mass can provide

**Table 6**  
Blue and Faint Red Fractions of Candidate Cluster Galaxies

Field	Redshift	$f_b$	$f_{fr}$
CL J0442+0202	$z = 1.10$	$40\% \pm 14\%$ ( $38\% \pm 29\%$ )	$25\% \pm 14\%$ ( $27^{+29}_{-27}\%$ )
3C 068.2	$z = 1.57$	$41\% \pm 18\%$ ( $27^{+33}_{-27}\%$ )	$26\% \pm 18\%$ ( $48\% \pm 33\%$ )
MS 1426.9+1052	$z = 1.83$	$49\% \pm 17\%$ ( $60\% \pm 33\%$ )	$24\% \pm 17\%$ ( $10^{+33}_{-10}\%$ )

**Note.** The blue ( $f_b$ ) and faint red fractions ( $f_{fr}$ ) of galaxies for each cluster candidate. Values in parentheses are the fractions contained within the regions of greatest galaxy overdensity ( $>10\sigma$ ). The blue fraction is calculated by using our  $z_f = 10$  CMR models for each cluster candidate (blue lines in Figure 8) which represents the expected red sequence at that redshift, and specifying the color cut as 0.2 mag bluer than the expected red sequence, following the example of Butcher & Oemler (1984). The probability distribution of each galaxy that falls below that color cut is deemed part of the blue fraction. The faint red fraction utilizes the same CMR line, and the color cut is 0.2 mag redder, with the additional constraint that each galaxy must be  $1.5 M_{5500}$  AB magnitudes fainter than the spectroscopic BCG in each cluster. Poissonian errors ( $\sqrt{N_{\text{obj}}}$ ) are included.

constraints on cosmological parameters and offer comparisons to simulations of large-scale structure. The leverage to constrain models improves with increasing mass and redshift. Further investigations into the properties of the constituent galaxies (morphology, colors, spectral signatures) will be facilitated by first establishing a quasi-virialized structure.

We would like to thank the anonymous referee for helpful comments. The work of S.S.M. is supported in part by NASA ADAP grant NNX11AF89G. This research has made use of the NASA/IPAC Extragalactic Database (NED) which is operated by the Jet Propulsion Laboratory, California Institute of Technology, under contract with the National Aeronautics and Space Administration. This publication makes use of data products from the 2MASS, which is a joint project of the University of Massachusetts and the Infrared Processing and Analysis Center/California Institute of Technology, funded by the National Aeronautics and Space Administration and the National Science Foundation.

## REFERENCES

- Baldry, I. K., Glazebrook, K., Brinkmann, J., et al. 2004, *ApJ*, 600, 681  
 Barthel, P., Haas, M., Leipski, C., & Wilkes, B. 2012, *ApJL*, 757, L26  
 Baum, W. A. 1959, *PASP*, 71, 106  
 Bell, E. F., Wolf, C., Meisenheimer, K., et al. 2004, *ApJ*, 608, 752  
 Bernardi, M., Sheth, R. K., Nichol, R. C., Schneider, D. P., & Brinkmann, J. 2005, *AJ*, 129, 61  
 Bertin, E., & Armouts, S. 1996, *A&AS*, 117, 393  
 Bower, R. G., Kodama, T., & Terlevich, A. 1998, *MNRAS*, 299, 1193  
 Bower, R. G., Lucey, J. R., & Ellis, R. S. 1992, *MNRAS*, 254, 601  
 Bregman, J. N., Temi, P., & Bregman, J. D. 2006, *ApJ*, 647, 265  
 Bruzual, G., & Charlot, S. 2003, *MNRAS*, 344, 1000  
 Butcher, H., & Oemler, A., Jr. 1984, *ApJ*, 285, 426  
 Cassata, P., Cimatti, A., Kurk, J., et al. 2008, *A&A*, 483, L39  
 Cassata, P., Giavalisco, M., Williams, C. C., et al. 2013, *ApJ*, 775, 106  
 Cen, R., & Ostriker, J. P. 1994, *ApJ*, 429, 4  
 Chang, R., Shen, S., Hou, J., Shu, C., & Shao, Z. 2006, *MNRAS*, 372, 199  
 Cooper, M. C., Newman, J. A., Weiner, B. J., et al. 2008, *MNRAS*, 383, 1058  
 Culverhouse, T. L., Bonamente, M., Bulbul, E., et al. 2010, *ApJL*, 723, L78  
 De Lucia, G., Springel, V., White, S. D. M., Croton, D., & Kauffmann, G. 2006, *MNRAS*, 366, 499  
 Dressler, A., Lynden-Bell, D., Burstein, D., et al. 1987, *ApJ*, 313, 42  
 Eisenhardt, P. R., De Propris, R., Gonzalez, A. H., et al. 2007, *ApJS*, 169, 225  
 Eisenhardt, P. R. M., Brodwin, M., Gonzalez, A. H., et al. 2008, *ApJ*, 684, 905  
 Ellis, R. S. 1988, in NATO ASIC Proc. 229, Cooling Flows in Clusters and Galaxies, ed. A. C. Fabian (Berlin: Springer), 305  
 Faber, S. M. 1973, *ApJ*, 179, 731  
 Faber, S. M., Willmer, C. N. A., Wolf, C., et al. 2007, *ApJ*, 665, 265  
 Fassbender, R., Nastasi, A., Santos, J. S., et al. 2014, *A&A*, 568, A5  
 Ferreras, I., Pasquali, A., Khochfar, S., et al. 2012, *AJ*, 144, 47  
 Fritz, A., Scodreggio, M., Ilbert, O., et al. 2014, *A&A*, 563, A92  
 Galametz, A., Stern, D., Stanford, S. A., et al. 2010, *A&A*, 516, A101  
 Gallazzi, A., Charlot, S., Brinchmann, J., & White, S. D. M. 2006, *MNRAS*, 370, 1106  
 Gavazzi, G., Pierini, D., Baffa, C., et al. 1996, *A&AS*, 120, 521  
 Gobat, R., Daddi, E., Onodera, M., et al. 2011, *A&A*, 526, A133  
 Gobat, R., Strazzullo, V., Daddi, E., et al. 2013, *ApJ*, 776, 9  
 Haas, M., Willner, S. P., Heymann, F., et al. 2009, *ApJ*, 695, 724  
 Hall, P. B., & Green, R. F. 1998, *ApJ*, 507, 558  
 Hall, P. B., Sawicki, M., Martini, P., et al. 2001, *AJ*, 121, 1840  
 Hogg, D. W., Blanton, M. R., Brinchmann, J., et al. 2004, *ApJL*, 601, L29  
 Kaviraj, S., Kirkby, L. A., Silk, J., & Sarzi, M. 2007, *MNRAS*, 382, 960  
 Keisler, R., Reichardt, C. L., Aird, K. A., et al. 2011, *ApJ*, 743, 28  
 Lee, K.-S., Dey, A., Hong, S., et al. 2014a, arXiv:1405.2620  
 Lee, S.-K., Ferguson, H. C., Somerville, R. S., et al. 2014b, *ApJ*, 783, 81  
 López-Cruz, O., Barkhouse, W. A., & Yee, H. K. C. 2004, *ApJ*, 614, 679  
 Madau, P., Ferguson, H. C., Dickinson, M. E., et al. 1996, *MNRAS*, 283, 1388  
 Mantz, A. B., Abdulla, Z., Carlstrom, J. E., et al. 2014, arXiv:1401.2087  
 McIntosh, D. H., Bell, E. F., Rix, H.-W., et al. 2005, *ApJ*, 632, 191  
 Mei, S., Holden, B. P., Blakeslee, J. P., et al. 2009, *ApJ*, 690, 42  
 Menanteau, F., Hughes, J. P., Sifón, C., et al. 2012, *ApJ*, 748, 7  
 Moore, B., Lake, G., Quinn, T., & Stadel, J. 1999, *MNRAS*, 304, 465  
 Mortonson, M. J., Hu, W., & Huterer, D. 2011, *PhRvD*, 83, 023015  
 Muchovej, S., Mroczkowski, T., Carlstrom, J. E., et al. 2007, *ApJ*, 663, 708  
 Newman, A. B., Ellis, R. S., Andreon, S., et al. 2014, *ApJ*, 788, 51  
 Overzier, R. A., Bouwens, R. J., Cross, N. J. G., et al. 2008, *ApJ*, 673, 143  
 Papovich, C. 2008, *ApJ*, 676, 206  
 Papovich, C., Bassett, R., Lotz, J. M., et al. 2012, *ApJ*, 750, 93  
 Papovich, C., Momcheva, I., Willmer, C. N. A., et al. 2010, *ApJ*, 716, 1503  
 Pérez-González, P. G., Rieke, G. H., Egami, E., et al. 2005, *ApJ*, 630, 82  
 Peter, A. H. G., Shapley, A. E., Law, D. R., et al. 2007, *ApJ*, 668, 23  
 Planck Collaboration, Ade, P. A. R., Aghanim, N., et al. 2013a, arXiv:1303.5062  
 Planck Collaboration, Ade, P. A. R., Aghanim, N., et al. 2013b, arXiv:1303.5080  
 Rakos, K. D., & Schombert, J. M. 1995, *ApJ*, 439, 47  
 Richards, G. T., Myers, A. D., Gray, A. G., et al. 2009, *ApJS*, 180, 67  
 Rozo, E., & Rykoff, E. S. 2014, *ApJ*, 783, 80  
 Schombert, J., & Rakos, K. 2009a, *AJ*, 137, 528  
 Schombert, J., & Rakos, K. 2009b, *ApJ*, 699, 1530  
 Sievers, J. L., Hlozek, R. A., Nolta, M. R., et al. 2013, *JCAP*, 10, 60  
 Steidel, C. C., Adelberger, K. L., Shapley, A. E., et al. 2005, *ApJ*, 626, 44  
 Stern, D., Holden, B., Stanford, S. A., & Spinrad, H. 2003, *AJ*, 125, 2759  
 Tecce, T. E., Cora, S. A., Tissera, P. B., Abadi, M. G., & Lagos, C. D. P. 2010, *MNRAS*, 408, 2008  
 Thomas, D., Maraston, C., Bender, R., & Mendes de Oliveira, C. 2005, *ApJ*, 621, 673  
 Tody, D. 1986, Proc. SPIE, 627, 733  
 Tody, D. 1993, in ASP Conf. Ser. 52, Astronomical Data Analysis Software and Systems II, ed. R. J. Hanisch, R. J. V. Brissenden & J. Barnes (San Francisco, CA: ASP), 173  
 Trager, S. C., Faber, S. M., Worthey, G., & González, J. J. 2000, *AJ*, 120, 165  
 van Dokkum, P. G., Franx, M., Kelson, D. D., & Illingworth, G. D. 1998, *ApJL*, 504, L17  
 Venemans, B. P., Kurk, J. D., Miley, G. K., et al. 2002, *ApJL*, 569, L11  
 Vikhlinin, A., Kravtsov, A. V., Burenin, R. A., et al. 2009, *ApJ*, 692, 1060  
 Visvanathan, N., & Sandage, A. 1977, *ApJ*, 216, 214  
 Wilkes, B. J., Kuraszkiewicz, J., Haas, M., et al. 2013, *ApJ*, 773, 15  
 Willis, J. P., Clerc, N., Bremer, M. N., et al. 2013, *MNRAS*, 430, 134  
 Wright, E. L. 2006, *PASP*, 118, 1711